

Latex films with gradients in crosslink density created by small-molecule-based auto-stratification

Heike Römermann and Diethelm Johannsmann^a

Institute of Physical Chemistry, Clausthal University of Technology 38678 Clausthal-Zellerfeld, Germany

Received 5 September 2018 and Received in final form 13 November 2018

Published online: 21 February 2019

© EDP Sciences / Società Italiana di Fisica / Springer-Verlag GmbH Germany, part of Springer Nature, 2019

Abstract. A suitable balance of convective and diffusive transport of small molecules contained in the liquid phase of a drying latex film leads to auto-stratification and to functionally graded films. Differing from blends of latex particles, which may also experience drying-induced segregation, small molecules retain their mobility after the particles have touched and have formed an elastically coupled network. The use of a thickener, which turns the dispersion into a weak gel and prevents the free flow of particles, is compatible with this approach (and even advantageous). A problem with small molecules is fast diffusive equilibration of concentration differences. For this reason, composition gradients along the lateral direction, where the characteristic length scale is centimeters, are more easily achieved than gradients along the vertical. Addition of a thickener slows down the diffusion, which aids the development of gradients along the vertical. The application example chosen was the crosslinking agent adipic dihydrazide, ADH, which takes part in keto-hydrazide coupling. Its heterogeneous distribution produces a spatially variable crosslink-density in the dry film as evidenced by Raman microscopy. A side aspect of the work is an *inward* flow of serum, which is observed for high- T_g films. An explanation for this “anti-coffee-ring effect” —based on pore collapse driven by the polymer-water interfacial energy combined with finite polymer elasticity— is proposed.

1 Introduction

Film formation from waterborne polymer dispersions certainly is complicated, but the different processes involved also open opportunities to influence the film’s final properties by a suitable drying protocol [1,2]. Among the targets of controlled drying is the spontaneous structure formation [3], well known from the coffee-ring effect [4,5]. The coffee-ring effect is of much importance in the drying of droplets (as in ink-jet printing) [6]. It is less relevant to planar films, but may still serve to study the balance between convective and diffusive transport. The coffee-ring effect has two separate consequences, which are *topographical features* (such as a bulge at the rim of a film or protrusions, where drying was fast) and spatially variable *composition* [7]. Well-defined topographical features have been created by evaporative lithography [8]. Compositional gradients generated by in-plane flow [9] are less common.

Composition gradients along the vertical are the consequence of auto-stratification (also: “self-stratification”). The prospect and the promises of auto-stratification have been recognized many years ago [10–14]. Ideally, stratified

films may replace multilayer films. This will save processing time, will avoid problems with adhesion between the different layers, and will allow for gradual changes in the materials properties (rather than abrupt changes at the boundaries between the different layers). Among the targets of functionally graded films are corrosion inhibition and scratch resistance [15]. Corrosion inhibition benefits from an enrichment of the active molecules at the bottom [16]. Scratch resistance benefits from a rigid surface with a more compliant medium underneath. The compliant medium dissipates energy, thereby preventing brittle fracture. Today the automotive industry uses dedicated “top-coats” (often composed of polyurethane, filled with nanoparticles) to achieve scratch resistance. Functionally graded materials can also serve this purpose. For example, the covers of modern mobile phones are made of a glass, which has undergone a chemical surface treatment *after* solidification, inducing a compressive stress at the surface [17]. Small scratches are prevented from growing because the material’s internal stress closes them. Various types of surface treatment in metal processing reduce wear along similar lines [18].

For very thin films, auto-stratification can be driven by interfacial energy [19]. In a film formed from a polymer

^a e-mail: johannsmann@pc.tu-clausthal.de

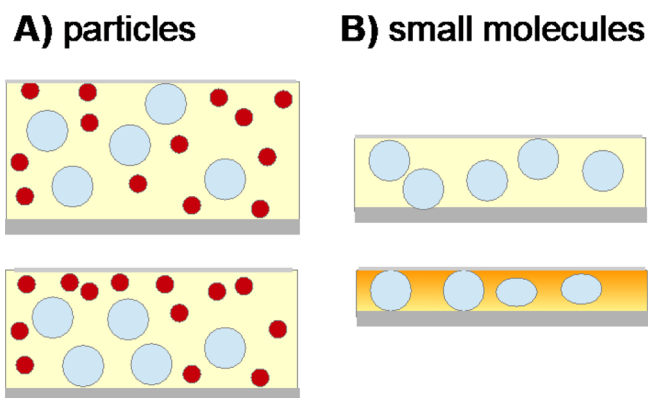


Fig. 1. (A) Stratification based on particles requires the dispersion to be in a fluid state. Otherwise, particles will not move relative to each other. This argument applies to both the small-on-top scenario (depicted here) and the large-on-top scenario. (B) Stratification based on serum components can operate after the particles have touched. Stratification is indicated as a color gradient along the vertical (bottom to top: yellow to red). The final state depicts the particle volume fraction as around 50% in order to let the color gradient of the background be visible. (More realistic would be 98%.) Particle size is not to scale.

blend, the more hydrophobic component often is enriched at the top. More advanced schemes employ surface-directed phase-separation [20]. Effects of surface tension do not usually suffice to achieve stratification in films with a thickness of tens of micrometers because surface tension only affects the near-surface range, the characteristic scale being of the order of size of a polymer coil [21]. For thicker films (such as the coatings used in the automotive industry, $d_{film} \sim 150 \mu\text{m}$), the prevalent methods to achieve stratification are based on nonequilibrium processes. As the water evaporates, there is convective transport of material (water, particles, serum components, ...) to the top. If some component diffusively equilibrates its concentration slower than another, a gradient in relative composition results (fig. 1). The slowly diffusing component is enriched at the top. Stratification in the final film is achieved, if this situation is frozen in, that is, if the motion arrests at a time when the fast components have equilibrated their concentration gradients, while the slow ones have not. Clearly, careful control of drying speed is required. While one might think, that the large particles would always be the slow particles and therefore would always be enriched at the top (“large-on-top” scenario), the opposite case (“small-on-top”) is observed, as well [22, 23]. The small-on-top situation results from interactions between large and small particles. Being more numerous than the large particles, the small particles develop an osmotic pressure and exert an entropic force onto the large particles, driving them to the bottom [24].

Auto-stratification based on colloidal particles requires particles moving relative to each other. This is in conflict with the common practice to employ dispersions with a high solids content and, also, added rheology modifiers. These turn the dispersion into a viscoplastic medium. Viscoelasticity prevents viscous flow after the film has been

applied, which avoids sagging and delays the sedimentation of pigments. At the same time, it lowers the self-diffusion coefficients of the particles. Small molecules are better suited to auto-stratification in this regard than particles, because they retain their mobility after the particles have touched to form an elastically coupled network. The price to be paid is the high diffusivity of small molecules. In order to achieve auto-stratification, a non-equilibrium situation needs to be frozen in, when the film turns dry. More technically, the time scale of drying, τ_{dry} , and the time scale of diffusion, τ_{diff} , must be similar. τ_{diff} is H^2/D with H the thickness of the film and D the diffusivity. The ratio of τ_{diff} and τ_{dry} is the “Peclet number”, Pe . Auto-stratification requires a Peclet number of the order of unity. The argument has been made more quantitative in terms of partial differential equation in refs. [25] and [26]. Importantly, the diffusivity depends on space and time. The diffusivity may vary over many decades, depending on the size of the molecule, the viscosity of the medium, and the presence of traps. Assuming a diffusivity of $D \sim 10^{-5} \text{ cm}^2/\text{s}$ (typical for ions in water) and a film thickness of $H \sim 100 \mu\text{m}$, one arrives at $\tau_{diff} \sim 10 \text{ s}$. Drying may be that fast in some industrial settings, but takes longer under most other circumstances. Small ions can then be expected to be evenly distributed along the vertical because diffusive equilibration is faster than drying. Again: This estimate was made for ions in water. As we will show below, an inhomogeneous distribution of serum components certainly can be achieved.

The results section has two parts. Section 3.1 reports results obtained using pH-sensitive dyes. These demonstrate that in-plane composition gradients based on small molecules are easily achieved. There is a dependence on the polymer’s glass temperature and on the presence of thickener. Gradients along the vertical can be achieved, as well. In sect. 3.2, we apply the concept to a polymer dispersion, which is designed to be crosslinked in the late stages of film formation by the keto-hydrazide mechanism [27, 28] (fig. 2). The polymer particles are functionalized with diacetone acrylamide (DAAM). The serum contains the crosslinking agent adipic dihydrazide (ADH) as well as ammonia, rendering it basic. Because the crosslinking reaction is catalyzed by H^+ , it does not proceed in the wet state. Ammonia evaporates slower than water, but it eventually evaporates, thereby lowering the pH of the nearly dry film. Crosslinking then sets in. It is essential that crosslinking occurs after the polymer chains have been given time to interdiffuse. Otherwise, films easily fracture [29, 30]. Crosslinks are found to be enriched close to the surface for high- T_g materials containing a thickener. In both cases (dyes and crosslinkers), the thickener takes a strong influence on auto-stratification.

2 Experimental

Acrylic latex dispersions were prepared by miniemulsion polymerization. Hexadecane (HD, Aldrich, 99%) was used as the co-stabilizer; azo-bis-isobutyronitrile (AIBN, Riedel-de Haën, recrystallized from diethyl ether) was the

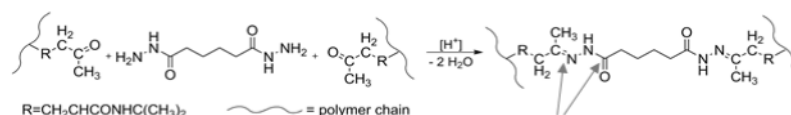


Fig. 2. The keto-hydrazone crosslinking mechanism. The functional group on the polymer (DAAM) is only shown in part. Blue arrows point to the imine group (only present after crosslinking) and the keto group. The ratio of the corresponding Raman bands was used to infer the degree of crosslinking (fig. 5).

initiator. Sonication of the monomer emulsion ensured a homogeneous droplet size. Polymerization took place at 70 °C for 20 hours. The solids content was 20 wt%. The diameter as determined by dynamic light scattering (DLS) varied between 80 and 120 nm, depending on the surfactant concentration.

Monomers were methyl methacrylate (MMA, Acros Organics, 99%) and *n*-butyl acrylate (BA, Aldrich, 99%). Diacetone acrylamide (DAAM, Aldrich, 99%) was added as a co-monomer (7 wt%) to those dispersions, which were intended for use in the crosslinking studies. Acrylic acid (AA) was not added to the recipe, as it is common practice otherwise. As reported in ref. [31], DAAM is more hydrophilic than the PMMA and PBA segments and therefore is preferentially located at the outside of the particles. Being hydrophilic, it stabilizes the dispersion. AA changes the *pH* which has numerous consequences being outside the scope of the work reported here. For reasons, which are further discussed in the supporting information, the latexes were all acidic. Sonication, degradation of SDS, and side products from the polymerization reaction are involved.

The glass temperatures, T_g , were set to -10 , 4 , and 21 °C (see fig. 3) by a suitably choice of the MMA/BA ratio. The T_g 's were calculated with the Fox equation, based on T_g 's of $+105$ °C and -54 °C for PMMA and PBA, respectively [32].

The dispersions designed to undergo crosslinking were stabilized against coagulation with the anionic surfactant sodium dodecyl sulfate (SDS, Aldrich, 98%). The dispersions prepared to study the transport of dyes and acid were stabilized with either SDS (Carl Roth > 99%) or the nonionic surfactant Lutensol AT50 (BASF). Lutensol AT50 is a block-copolymer with a PEG-chain of about 50 ethoxy-groups being the hydrophilic part.

The dispersions formulated for crosslinking were rendered basic (*pH* 9) by addition of ammonia solution (Merck, 28–30%). Adipic dihydrazide (ADH, TCI, > 99%) was added to the serum as a 10-wt%, aqueous solution in a ratio of 1/7 v/v to the dispersion, setting the ADH/DAAM ratio to 1:2.

An associative thickener (Tafigel PUR60, Münzing, Germany) was employed in some cases [33]. Tafigel PUR60 is a triblock-copolymer, where the middle blocks consist of polyurethane and the chain ends are hydrophobic (a hydrophobically modified ethoxylated urethane copolymer, HEUR). The chain ends weakly adsorb to the particle surface, thereby creating a gel. Concentrations were 0.1, 0.3, and 0.5 wt%.

Raman maps were acquired with a Senterra Raman microscope (Bruker). The laser wavelength was 532 nm. The

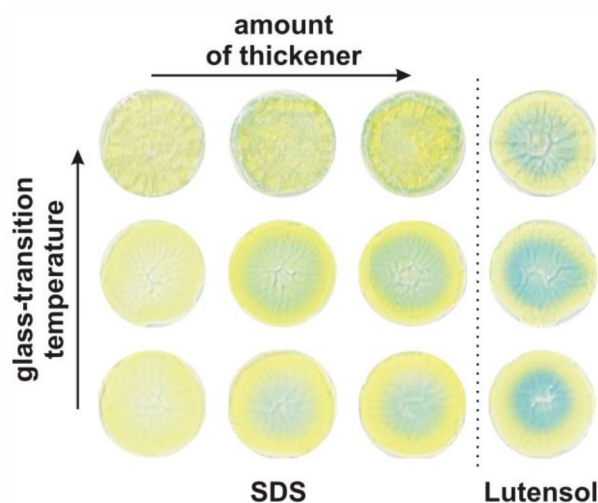


Fig. 3. In-plane gradients in color of a *pH*-indicator are readily observed under a wide variety of drying conditions and material parameters. The diameter of the films was 12 mm.

microscope's resolution along the *z*-direction was inferred to be about 30 μm from the strength of a vibration band originating from silicon (which was the substrate in these experiments). As the focus moves vertically away from the substrate into the film, the intensity of this band decreases exponentially, the $1/e$ -height being 30 μm . In the experiments using conventional dyes, the color distribution was studied with optical microscopy. Color distributions along the vertical were obtained by sectioning slices out of the film and imaging these side-on.

As a small molecule for reference experiments, we chose the *pH*-indicator bromothymol blue (Fluka). The color of this dye changes from yellow (acidic) to blue (basic) at *pH* 7. Bromothymol blue was first dissolved in deionized water at a concentration of 1 wt%. This solution was added to the serum at a ratio of 1/9 v/v.

Films were prepared as circular disks with a diameter of 12 mm by masking the glass substrate with adhesive tape and cutting holes into these. The circular geometry ensured that the in-plane flow occurred into the radial direction. The dry film thickness was 160 μm .

3 Results

3.1 Gradients in color of *pH*-indicators

Figure 3 shows a set of images taken on dry films from the top. The samples on the left-hand side were produced from dispersions stabilized with the anionic surfactant

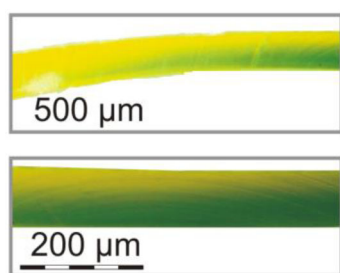


Fig. 4. Images of vertical cuts through the film. While there are color gradients, they vary with position. The conditions were $T_g = 4^\circ\text{C}$, 0.3 wt% thickener, emulsifier: SDS.

SDS. The concentration of thickener increases from left to right (0.0%, 0.3%, 0.5%). The glass temperature as calculated from the Fox equation increases from the bottom to the top ($T_g = -10, 4,$ and 21°C). The images on the right-hand side show samples containing the nonionic surfactant Lutensol AT50 as the emulsifier. These samples do not contain a thickener. The glass temperature increases from bottom to top.

In most cases, the centers are less colored than the rim, which we interpret in terms of dye molecules being carried towards the edge. The color of the dye changes from blue ($\text{pH} > 7$) close to the center to yellow ($\text{pH} < 7$) at the edge. Acid has been carried to the edge, as well. From the fact that the transition between acidic and basic occurs about half-way from the center to the edge, one concludes that the transport was faster for the acidic molecules than for the dye itself. Presumably, this effect goes back to size. The molar mass of SDS is 288 g/mol , to be compared to 624 g/mol for bromothymol blue. Larger molecules are more easily trapped.

The high- T_g samples stabilized with SDS behave differently from the low- T_g samples. The center does not turn blue. Actually, the high- T_g samples containing the thickener display a blue ring at the edge. Acid has been carried from the edge towards the center. A similar finding was reported in ref. [34]. When high- T_g samples dry, they often show a drying front moving inwards from the edge. The drying front is caused by an instability. The liquid-filled interstitial volume collapses, driven by the interfacial energy between water and polymer [35]. The collapse pumps liquid inwards (contrasting to what is known from the coffee-ring effect). Presumably, a similar process occurred with the high- T_g SDS-stabilized samples shown at the upper left in fig. 3. This effect does not occur with the Lutensol-stabilized high- T_g sample on the top-right. It is known, that Lutensol acts as plasticizer, lowering the T_g [36]. Lowered T_g , compared to the SDS-stabilized samples, can explain this effect. This argument is made more quantitative in the appendix.

The SDS-stabilized samples require a thickener for the formation of pH -gradients. One may envision the thickener as a network, which impedes diffusion. Slowing down diffusion brings the Peclet number for lateral transport into the required range ($Pe \approx 1$). The latexes stabilized with the nonionic surfactant do not require the addition

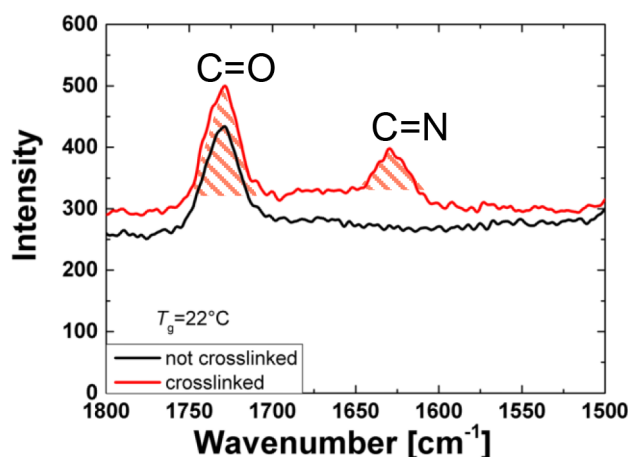


Fig. 5. The degree of crosslinking was inferred from the ratio of two Raman bands, which are the imine band at 1750 cm^{-1} and the carbonyl band at 1630 cm^{-1} .

of a thickener because the long diblock-copolymer chains of Lutensol AT50 take the same role.

Side-on images of cross-sections are displayed in fig. 4. The T_g of these samples was 4°C . They contained 0.3 wt% thickener. As expected, the top is more acidic than the bottom. Clearly, auto-stratification has not been achieved everywhere to the same extent. Presumably this goes back to slightly different drying rates at the different positions. Convection roles as reported in ref. [37] may also play a role.

3.2 Gradients in crosslink density

While the experiments with dyes demonstrate auto-stratification as such, dyes are of limited practical importance. A more relevant molecule is, for instance, a crosslinker, which we chose to be adipic dihydrazide, ADH. ADH reacts with carbonyl groups exposed at the surface of the sphere. An gradient in crosslink-density may be beneficial for scratch resistance. The degree of crosslinking was assessed from the relative intensities of two Raman bands (fig. 5), namely the carbonyl band (1750 cm^{-1}) and the imine band (1630 cm^{-1}). The keto-hydrazide reaction couples a carbonyl-group to a hydrazide-group, eliminating water and forming an imine bond (fig. 2).

Figure 6 shows the imine-to-carbonyl ratio *versus* distance from the center for a soft sample ($T_g = 10^\circ\text{C}$) containing 0.5% thickener (similar to the third sample from the left in the bottom row of fig. 3). The crosslink density near the edge is higher than near the center, which matches the observation made with bromothymol blue. Figure 7 displays the same ratio *versus* vertical position. An increase in crosslink density is observed for the high- T_g sample containing thickener. (No such effect occurred for soft samples. The cross-link density even had decreased close to the surface for some low- T_g -samples.) There is a dependence on particles size. The effect was more pronounced for the sample with slightly larger particles. Note that the point-spread function of the microscope along the optical axis z has an effective radius of

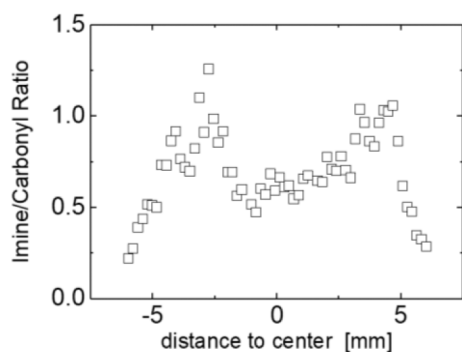


Fig. 6. Horizontal Raman-map of a dried latex film with $T_g = -10^\circ\text{C}$ containing 0.5% thickener.

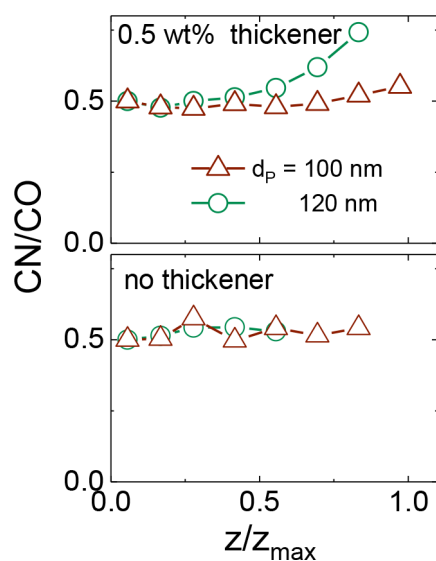


Fig. 7. Dependence of crosslink density on vertical position inside the film as inferred from the ratio of the imine to the carbonyl band with Raman profilometry.

$30\ \mu\text{m}$. Possibly, the extrema of the crosslink density at the film surface have been smeared out by the microscope's finite z -resolution. No increase in crosslink density is observed for samples not containing a thickener. This finding matches the observation from fig. 3. A thickener is needed to slow down the diffusion of the crosslinking agent ADH, so that the time scales of diffusion and drying match.

4 Conclusions

Flow of water during drying of a polymer latex leads to compositional gradients of the serum components. The approach is technically attractive because it can be applied to latexes with a high solids content and with added thickeners. Composition gradients in the dry film require the Peclet number to be of the order of unity. The Peclet number tends to be below unity for small molecules because of fast diffusion. For larger molecules—like dyes or the crosslinking agent ADH—the addition of thickener slows down diffusion and can bring the Peclet number into the required range.

Composition gradients both in the plane of the film and along the vertical have been found for latex films containing pH-sensitive dyes and films containing a crosslinking agent. There were dependences on both the glass temperature and the concentration of added thickener. Increased levels of crosslinking at the top of a film—as desired for scratch-resistant coatings—have been achieved for materials with a high- T_g containing thickener.

We acknowledge support by Karin Bode with confocal Raman microscopy (Institute of Inorganic and Analytical Chemistry, Clausthal).

Author contribution statement

HR performed the experiments and contributed to writing. DJ designed much of the experiment and wrote the paper.

Publisher's Note The EPJ Publishers remain neutral with regard to jurisdictional claims in published maps and institutional affiliations.

Appendix A. A justification for pore collapse driving material inwards for latex films composed of high- T_g polymers

With latex films containing particles with T_g near room temperature, one frequently observes an *inward* movement of liquid [34,38]. The features discussed in ref. [35] can also be discerned in the images shown in ref. [39]. Part of the key figure from ref. [34] is reproduced in fig. 8 for completeness. This behavior is opposite to the more commonly observed “coffee-ring effect”, which implies an *outward* movement.

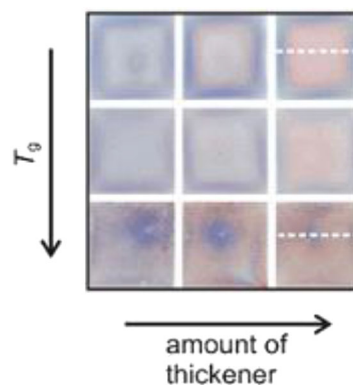


Fig. 8. Images of dry films, which had been stained with congo red (a pH-sensitive dye, which is blue and red in acidic and alkaline environments, respectively). The dry film thickness was $80\ \mu\text{m}$. The T_g 's of the polymer were -10°C , 4°C , and 20°C at the top, the centre, and the bottom, respectively. The amount of thickener was 0% (left), 0.5% (centre) and 1.5% (right). Adapted from ref. [34].

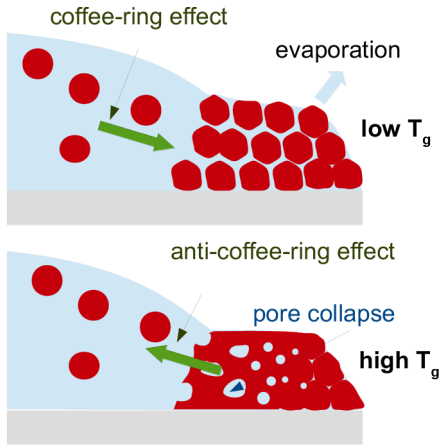


Fig. 9. A sketch of the mechanism behind the anti-coffee-ring effect. The top graph was adapted from ref. [39], where ref. [39] does specifically address softness. The model proposed here suggests, that this argument is only applicable to soft particles. For high- T_g particles, one finds an inward flow, caused by pore-collapse.

The collapse of a porous network under the capillary pressure exerted by the polymer-water interface amounts to an instability, driven by wet sintering (fig. 9). The instability is related to the Rayleigh instability in liquid jets. Pores differ from liquid jets in that there is a no-slip condition at the liquid-polymer interface, which leads to a viscous drag. The model assumes both the polymer phase and the serum to behave as liquids (albeit with vastly different viscosities). The large pores grow at the expense of the small pores until the small pores eventually close. *However, this Rayleigh-like instability is suppressed by the hydrodynamic drag for low T_g -samples.* This argument is made quantitative in the following.

Start from Darcy's law, which states that

$$v = -\frac{\kappa}{\eta} \nabla p = -\frac{r^2}{\eta} \nabla p \quad (\text{A.1})$$

v is the velocity, κ is the permeability, η is the viscosity of the liquid, and p is the pressure. The permeability has units of an area and is of the order of the cross-sectional area of the pores. κ was replaced by r^2 in the second step, where r is some effective radius.

For the sake of the argument, replace the porous medium by a single, conical pore with length L and opening radius r_0 (fig. 10). Let the pressure be dominated by capillarity

$$p_{cap} = \frac{\gamma}{r}. \quad (\text{A.2})$$

Inserting eq. (A.2) into eq. (A.1) yields

$$v = -\frac{r^2}{\eta} \nabla \left(\frac{\gamma}{r} \right) = \frac{\gamma}{\eta} \nabla r. \quad (\text{A.3})$$

Assume the initial condition as

$$r_{ini}(x) = r_0 \left(1 - \frac{x}{L} \right). \quad (\text{A.4})$$

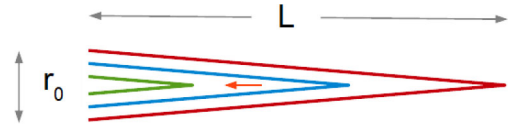


Fig. 10. If pressure is dominated by capillarity and if the pore is cone-shaped initially, Darcy's equation predicts an affine shrinkage of the pore. There is no front, at which the pore would discontinuously collapse.

Volume conservation demands

$$\begin{aligned} \frac{d(\pi r^2)}{dt} &= -\frac{dQ}{dx} = -\frac{d}{dx} (\pi r^2 v) \\ &= -2\pi r \frac{dr}{dx} v - \pi r^2 \frac{dv}{dx} \end{aligned} \quad (\text{A.5})$$

πr^2 is the cross section of the pore; Q is the flux. Inserting v from eq. (A.3), one finds

$$2\pi r \frac{dr}{dt} = -2\pi r \frac{\gamma}{\eta} \left(\frac{dr}{dx} \right)^2 - \pi r^2 \frac{\gamma}{\eta} \frac{d^2 r}{dx^2} \quad (\text{A.6})$$

and

$$\frac{dr}{dt} = -\frac{\gamma}{\eta} \left(\left(\frac{dr}{dx} \right)^2 + \frac{r}{2} \frac{d^2 r}{dx^2} \right). \quad (\text{A.7})$$

With the initial conditions from eq. (A.4), the second term is zero. The first term is constant and given as $(r_0/L)^2$. The pore therefore continuously shrinks:

$$r(x, t) = \max \left(r_{ini}(x) - \frac{\gamma}{\eta} \left(\frac{r_0}{L} \right)^2 t, 0 \right). \quad (\text{A.8})$$

The condition $r(x, t) \geq 0$ reflects that the above argument breaks down at the molecular scale. Equation (A.8) implies a characteristic time of pore closure given as $r_{ini} \eta L^2 / (\gamma r_0^2)$.

Key to the argument is that the pore's cross sectional area in eq. (A.3) cancels against the $1/r^2$ -term resulting from the derivative of γ/r . The initial condition has been chosen to allow for an analytical solution, but the argument as such does not depend on the initial condition: The large frictional drag inside small pores opposes the collapse (opposes the Rayleigh instability), which would otherwise set in.

Now let the polymer medium have a finite elastic stiffness. From dimensional arguments, the resulting pressure must be given as

$$p_{elas} = -\frac{r_{ini} - r}{r_{ini}} G. \quad (\text{A.9})$$

Only this form yields the correct dimension and linear behavior at $r \approx r_{ini}$. G is an effective modulus, proportional to the shear modulus. The velocity resulting from Darcy's law is

$$\begin{aligned} v &= -\frac{r^2}{\eta} \nabla \left(\frac{\gamma}{r} - G \frac{r_{ini} - r}{r_{ini}} \right) = \left(\frac{\gamma}{\eta} - \frac{r^2 G}{r_{ini} \eta} \right) \nabla r \\ &= \left(\frac{\gamma}{\eta} - \frac{r^2}{r_{ini} \tau} \right) \nabla r. \end{aligned} \quad (\text{A.10})$$

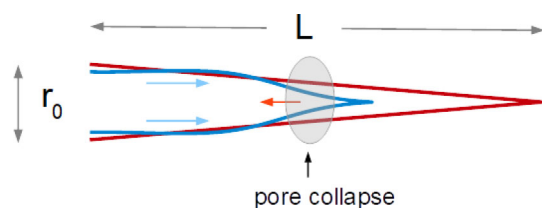


Fig. 11. A finite elasticity of the polymer phase introduces a flow into the reverse direction, adding onto the flow caused by capillarity. The latter flux is large at large pore diameters.

In the second step, the ratio η/G was renamed as τ (a relaxation time).

The elastic stress results in a reverse flow, which is large at large r (fig. 11). One may insert eq. (A.10) into eq. (A.4) and arrive at an equation, the numerical solution of which confirms what is drawn in fig. 11. However, the quantitative treatment requires close attention to a suitable choice of parameters in order to avoid instabilities. For a realistic, quantitative treatment, one should simulate a porous network with branches and a pore size distribution. Such a treatment is outside the scope here. We leave it with the argument from eq. (A.10) and fig. 11. This work is by no means a comprehensive theory of the anti-coffee-ring effect. An elastic stress breaks the cancellation between large capillary stresses and large hydrodynamic resistance, which is found, if capillarity is the only source of a pressure. For that reason, a collapse front moving from the rim of a sample towards the center is only found with the high- T_g samples.

This leaves the question of why pore collapse would progress from the rim to the center (and not the other way round). Pore collapse is nucleated at the rim, because drying is faster there, initially. This initial condition provides for the asymmetry required by the argument.

The bracket on the right-hand side in eq. (A.10) can be used to estimate a minimum pore radius. Because of $r \leq r_{ini}$, the condition for reverse flow may be phrased as

$$0 > \frac{\gamma}{\eta} - \frac{r_{ini}^2}{r_{ini}\tau} \Rightarrow r_{ini} > \frac{\gamma}{G}. \quad (\text{A.11})$$

The definition of τ as η/G was used in the second step. Using (for example) $\gamma \approx 10^{-2} \text{ J/m}^2$ and $G \approx 10^6 \text{ Pa}$ leads to $r_{min} > 10 \text{ nm}$. These are realistic values for drying latex dispersions.

The scenario outlined above is distinctly different from another chain of events, also leading to inward flow. If a skin forms at the rim of a droplet, it may slow down evaporation there. The rate of evaporation then is largest in the center, which may cause a movement of polymer material towards the center (as in the case of the coffee-ring effect, the difference being that evaporation is fast in the center). Skin formation, however, is expected for soft polymers, not for high- T_g polymers. Skin formation setting in at the rim might explain the findings from ref. [40], at least in principle.

References

1. J.L. Keddie, A.F. Routh, *Fundamentals of Latex Film Formation: Processes and Properties* (Springer, 2010).
2. M.A. Winnik, *Curr. Opin. Colloid Interface Sci.* **2**, 192 (1997).
3. P. Bacchin, David B. Brutin, A. Davaille, E. Di Giuseppe, X.D. Chen, I. Gergianakis, F. Giorgiutti-Dauphiné, L. Goehring, Y. Hallez, R. Heyd, R. Jeantet, C. Le Floch-Fouéré, M. Meireles, E. Mittelstaedt, C. Nicloux, L. Pauchard, M.-L. Saboungi, *Eur. Phys. J. E* **41**, 94 (2018).
4. R.D. Deegan, O. Bakajin, T.F. Dupont, G. Huber, S.R. Nagel, T.A. Witten, *Nature* **389**, 827 (1997).
5. W. Han, Z.Q. Lin, *Ang. Chemie Int. Ed.* **51**, 1534 (2012).
6. A.D. Eales, N. Dartnell, S. Goddard, A.F. Routh, *J. Colloid Interface Sci.* **458**, 53 (2015).
7. A.A.F. Georgiadis, M.W. Murray, J.L. Keddie, *Soft Matter* **7**, 11098 (2011).
8. D.J. Harris, H. Hu, J.C. Conrad, J.A. Lewis, *Phys. Rev. Lett.* **98**, 148301 (2007).
9. D.J. Harris, J.C. Conrad, J.A. Lewis, *Philos. Trans. R. Soc. A: Math. Phys. Eng. Sci.* **367**, 5157 (2009).
10. K.L. Rhudy, S. Su, H.R. Howell, M.W. Urban, *Langmuir* **24**, 1808 (2008).
11. V.V. Verkholantsev, *Pigment Resin Technol.* **32**, 300 (2003).
12. M.W. Urban, *Eur. Coat. J.* **1–2**, 36 (2003).
13. D.J. Walbridge, *Prog. Organic Coat.* **28**, 155 (1996).
14. H. Luo, C.M. Cardinal, L.E. Scriven, L.F. Francis, *Langmuir* **24**, 5552 (2008).
15. B.J. Briscoe, S.K. Sinha, *Materialwiss. Werkstofftech.* **34**, 989 (2003).
16. G. Grundmeier, B. Rossenbeck, K.J. Roschmann, P. Ebbinghaus, M. Stratmann, *Corros. Sci.* **48**, 3716 (2006).
17. https://en.wikipedia.org/wiki/Gorilla_Glass.
18. E.J. Mittemeijer, M.A.J. Somers, *Thermochemical Surface Engineering of Steels: Improving Materials Performance* (Woodhead Publishing, 2014).
19. C. Carr, E. Wallstom, *Prog. Organic Coat.* **28**, 161 (1996).
20. R.A.L. Jones, L.J. Norton, E.J. Kramer, F.S. Bates, P. Wiltzius, *Phys. Rev. Lett.* **66**, 1326 (1991).
21. A. Budkowski, F. Scheffold, J. Klein, L.J. Fetters, *J. Chem. Phys.* **106**, 719 (1997).
22. A. Fortini, I. Martin-Fabiani, J.L. De La Haye, P.Y. Dugas, M. Lansalot, F. D'Agosto, E. Bourgeat-Lami, J.L. Keddie, R.P. Sear, *Phys. Rev. Lett.* **116**, 118301 (2016).
23. Y.F. Tang, G.S. Grest, S.F. Cheng, *Langmuir* **34**, 7161 (2018).
24. J. Zhou, Y. Jiang, M. Doi, *Phys. Rev. Lett.* **118**, 108002 (2017).
25. A.F. Routh, W.B. Zimmerman, *Chem. Eng. Sci.* **59**, 2961 (2004).
26. R.E. Trueman, E.L. Domingues, S.N. Emmett, M.W. Murray, A.F. Routh, *J. Colloid Interface Sci.* **377**, 207 (2012).
27. J.W. Taylor, M.A. Winnik, *JCT Res.* **1**, 163 (2004).
28. J.L. Keddie, N. Kessel, D.R. Illsley, *J. Coat. Technol. Res.* **5**, 285 (2008).
29. S.S. Voyutskii, Z.M. Ustinova, *J. Adhes.* **9**, 39 (1977).
30. P. Bakker, D. Mestach, *Surf. Coat. Int. B* **84**, 271 (2001).
31. C.G. Koukiotis, M.M. Karabela, I.D. Sideridou, *Prog. Org. Coat.* **75**, 106 (2012).
32. J. Brandrup, E.H. Immergut, E.A. Grulke, *Polymer Handbook*, 4th edition (Wiley, Hoboken, 1999).

33. Münzing GmbH, Rheology Modifiers TAFIGEL product description, https://www.munzing.com/fileadmin/_migrated/content_uploads/TAFIGEL-PUR-Rheology-Modifiers_01.pdf (09.08.2018).
34. M. Schulz, H. Römermann, K. Pohl, C. Chindawong, D. Johannsmann, *Soft Mater.* **13**, 138 (2015).
35. K. Pohl, R. König, H. Römermann, M. Schulz, D. Johannsmann, *Langmuir* **30**, 9384 (2014).
36. S.T. Eckersley, A. Rudin, *J. Appl. Polym. Sci.* **48**, 1369 (1993).
37. P. Vink, T.L. Bots, *Prog. Org. Coat.* **28**, 173 (1996).
38. M. Schulz, H. Römermann, K. Pohl, C. Chindawong, D. Johannsmann, *Soft Mater.* **13**, 138 (2015).
39. L. Goehring, W.J. Clegg, A.F. Routh, *Langmuir* **26**, 9269 (2010).
40. L. Pauchard, C. Allain, *Europhys. Lett.* **62**, 897 (2003).